Journal of Rock Mechanics and Geotechnical Engineering 16 (2024) 924–941

Contents lists available at ScienceDirect

Journal of Rock Mechanics and Geotechnical Engineering

journal homepage: www.jrmge.cn

Full Length Article

A method to interpret fracture aperture of rock slope using adaptive shape and unmanned aerial vehicle multi-angle nap-of-the-object photogrammetry

Mingyu Zhao [a], Shengyuan Song [a,*], Fengyan Wang [b], Chun Zhu [c], Dianze Liu [a], Sicong Wang [a]

[a] College of Construction Engineering, Jilin University, Changchun, 130026, China
[b] College of Geo-Exploration Science and Technology, Jilin University, Changchun, 130026, China
[c] Institute of Engineering Geology and Geohazards, Hohai University, Nanjing, 210098, China

ARTICLE INFO

Article history:
Received 29 December 2022
Received in revised form
14 May 2023
Accepted 9 July 2023
Available online 12 September 2023

Keywords:
Unmanned aerial vehicle (UAV)
photogrammetry
High-steep rock slope
Fracture aperture
Interval effect
Size effect
Parameter interpretation

ABSTRACT

The aperture of natural rock fractures significantly affects the deformation and strength properties of rock masses, as well as the hydrodynamic properties of fractured rock masses. The conventional measurement methods are inadequate for collecting data on high-steep rock slopes in complex mountainous regions. This study establishes a high-resolution three-dimensional model of a rock slope using unmanned aerial vehicle (UAV) multi-angle nap-of-the-object photogrammetry to obtain edge feature points of fractures. Fracture opening morphology is characterized using coordinate projection and transformation. Fracture central axis is determined using vertical measuring lines, allowing for the interpretation of aperture of adaptive fracture shape. The feasibility and reliability of the new method are verified at a construction site of a railway in southeast Tibet, China. The study shows that the fracture aperture has a significant interval effect and size effect. The optimal sampling length for fractures is approximately 0.5–1 m, and the optimal aperture interpretation results can be achieved when the measuring line spacing is 1% of the sampling length. Tensile fractures in the study area generally have larger apertures than shear fractures, and their tendency to increase with slope height is also greater than that of shear fractures. The aperture of tensile fractures is generally positively correlated with their trace length, while the correlation between the aperture of shear fractures and their trace length appears to be weak. Fractures of different orientations exhibit certain differences in their distribution of aperture, but generally follow the forms of normal, log-normal, and gamma distributions. This study provides essential data support for rock and slope stability evaluation, which is of significant practical importance.

1. Introduction

Discontinuities are widely distributed in rock masses and play a significant role in controlling the deformation and damage of the rock mass (Azarafza et al., 2017; Bostanci et al., 2018). Therefore, the comprehensive study of discontinuity properties is crucial for all types of rock engineering (Hammah and Curran, 1998; Zheng et al., 2014; Cui et al., 2022). Accurately and efficiently obtaining parameters of rock structures is particularly vital for practical applications (Einstein et al., 1983; Eshiet and Sheng, 2017; Li et al., 2017). Among various parameters of rock structures, fracture aperture is an essential indicator that describes the opening properties of discontinuities and is the most challenging to measure (Sun et al., 2020; Liu et al., 2021a). In addition to directly influencing the deformation and strength properties of rock masses, fracture aperture significantly controls the hydrodynamic properties of fractured rock masses (Gong and Rossen, 2017; Frash et al., 2019). Thus, the study of natural rock fracture aperture is of significant practical importance for rock engineering (Wu et al., 2021).

Currently, the investigation methods for fracture aperture mainly include two types: field investigation (ISRM, 1978) and indoor investigation (Kumar et al., 1997; Li et al., 2021; Reinhardt et al., 2022). Field investigation involves measuring the rock directly with feeler gauges or millimeter rulers. While this method is relatively simple, it is inefficient and vulnerable to subjective

* Corresponding author.
E-mail address: songshengyuan@jlu.edu.cn (S. Song).
Peer review under responsibility of Institute of Rock and Soil Mechanics, Chinese Academy of Sciences.

https://doi.org/10.1016/j.jrmge.2023.07.010

influences from the observer performing measurements. Moreover, the method is restricted by topography, making it challenging to measure fracture aperture on steep slopes. Indoor investigation mainly includes casting method (Hakami and Barton, 1990; Yeo et al., 1998), injection method (Tsang and Tsang, 1990; Hakami and Stephansson, 1993), surface morphology method (Iwano and Einstein, 1993), nuclear magnetic resonance (NMR) method (Xiao and Li, 2011), computer aided tomography (CAT) (Keller, 1998), and digital image processing technology (Mazumder et al., 2006; Torkan et al., 2022). This type of method mainly uses rock samples collected on-site or self-made samples and specialized equipment to obtain fracture aperture information (Gentier, 1990). Its advantages lie in the ability to replicate or restore the morphology of fractures and the high accuracy of interpretation (Liu et al., 2021b). However, this type of method requires expensive equipment, complex operation procedures, and special requirements for the shape and size of rock samples (Song et al., 2021). With the continuous expansion of various rock engineering projects in terms of scale and quantity, higher demands have been placed on the acquisition of rock mass structural parameters (Bostanci et al., 2018; Zhan et al., 2021; Lan et al., 2022). Due to the inaccessibility of high-steep slopes, both field investigation and indoor investigation methods cannot meet the technical requirements of modern rock engineering for rapid construction. Therefore, there is an urgent need to research a new non-contact method for identifying and interpreting fine parameters of rock mass fractures.

In recent years, unmanned aerial vehicle (UAV) technology has become more mature, with significant improvements in attitude control and sensor performance (Johansen et al., 2019; Rahman et al., 2021; Xiu et al., 2021). This has enabled the use of UAV technology to acquire high-resolution images and interpret fine parameters of rock mass structure (Salvini et al., 2020). Lopes et al. (2022) employed UAV photogrammetry to obtain fracture aperture from orthophoto images of the study area. However, this method is limited in that it can only identify crack aperture on the horizontal plane and is unable to account for cracks on the side of the slope. This method is unable to interpret discontinuity orientation, resulting in limited types of obtainable rock mass structural parameters (Salvini et al., 2017; Bar et al., 2021). This indicates that the conventional UAV photography cannot fully meet the requirements of explaining the fine parameters of rock mass structure in high-steep slopes (Liu et al., 2022). Due to the limited research on fracture aperture measurement using UAV technology, further investigation is necessary to optimize UAV photography for identifying and interpreting complex structures on high-steep slopes. Additionally, exploring a new method for interpreting fracture aperture based on high-resolution UAV image is necessary for practical engineering applications.

This study proposes a UAV multi-angle nap-of-the-object photogrammetry that fully considers the terrain features of complex structures on high-steep slopes and the geometric characteristics of developed discontinuities, based on conventional UAV nap-of-the-object photogrammetry. A new method is presented for the identification and interpretation of linear discontinuities based on high-resolution three-dimensional (3D) real scene models of slopes. The aperture values are automatically calculated and analyzed in batches based on the edge feature points of the fracture, which is implemented through programming. In addition, the interval effect, size effect, probability distribution characteristics of fracture aperture in the study area, as well as their relationship with trace length and slope altitude, are investigated. This study has important practical engineering significance for the rapid acquisition of fine parameters of high-steep rock slopes, as well as the evaluation of slope stability and block stability.

2. Study area

The research area is located in Xiali Township of Changdu City, Tibet Autonomous Region, China (Fig. 1a), and is characterized by a typical mountain-canyon geomorphology. The valley exhibits a typical V-shaped cross-sectional profile, and the vertical variation of the terrain is quite significant. The lowest point is about 3300 m above sea level and the highest point is about 4000 m above sea level. The strata exposed in the study area are mainly the Quaternary, the Jurassic, Triassic of the Mesozoic era, and the Permian of the Paleozoic era. The lithology of the strata mainly consists of three formations. The Middle Jurassic Marix Formation (J_2m) is dominated by grey conglomeratic sandstone, purple-red conglomerate, and thinly interbedded grey limestone. The Upper Triassic Guzhutong Formation (T_3gz) is mainly composed of light grey siliceous banded limestone, siliceous rock, and shale. The Permian Xijikar Formation (Pz_2xj) is primarily composed of muscovite quartz schist, sodic greenish-brown clayey schist, crystalline limestone, and quartzite (Huo, 2020) (Fig. 1b).

The Dalong-Basu Fault is developed in the study area, which is a large regional fault with a northwest bending extension. The fault fragmentation zone is about 200 m wide, and there are extrusion fragmentation zones ranging from 50 m to 350 m. Influenced by the uplift of the Himalayas, the tectonic stress in the study area gradually increases, and seismic activity is frequent. The seismic intensity in the study area is VIII, which is a medium-intensity seismic zone (Shi et al., 2021). The area is controlled by the climate of the Tibetan Plateau, with dry weather and low rainfall. The Walayong river passes through the study area from south to north and is mainly recharged by rainfall and snow melt water. The loose rock pore water is mainly stored in the alluvium, alluvium, broken residual layer, and moraine layer of the Quaternary System (Shi, 2021).

On-site investigations revealed that the overall strike of the slope is approximately NE22°, with a slope angle of 51° and a height of 575 m (Fig. 1c). The lithology of the slope location is mainly composed of conglomerate and limestone. The slope develops a large number of discontinuities, which can be roughly divided into four sets, among which the steeply dipping discontinuities with a dip direction of 45° are the most developed. The rock mass exhibited a blocky structure. The slope bottom is close to a river, and the groundwater level is relatively high. The development of laminated or platy structure in the rock mass facilitated the infiltration and dissolution of water, resulting in the discovery of multiple karst phenomena at the slope bottom (Fig. 1d). A debris flow gully with a large watershed area is developed in the western part of the study area, which often causes different degrees of debris flow hazards to the downstream.

A railway is planned to be built in the study area, and a Xiali bridge will be constructed in the eastern gully to connect the tunnels on both sides. Investigating the stability of the rock mass above the tunnel entrance and analyzing the disaster-causing mechanism of high-level hidden collapse and rock fall are critical to the management and safe operation of the railroad. There is an urgent need for new and reliable methods to rapidly obtain structural parameters of rock masses for slope and block evaluation and analysis. This study aims to provide a new method for interpreting the aperture of fractures in complex and steep rock slopes in rock

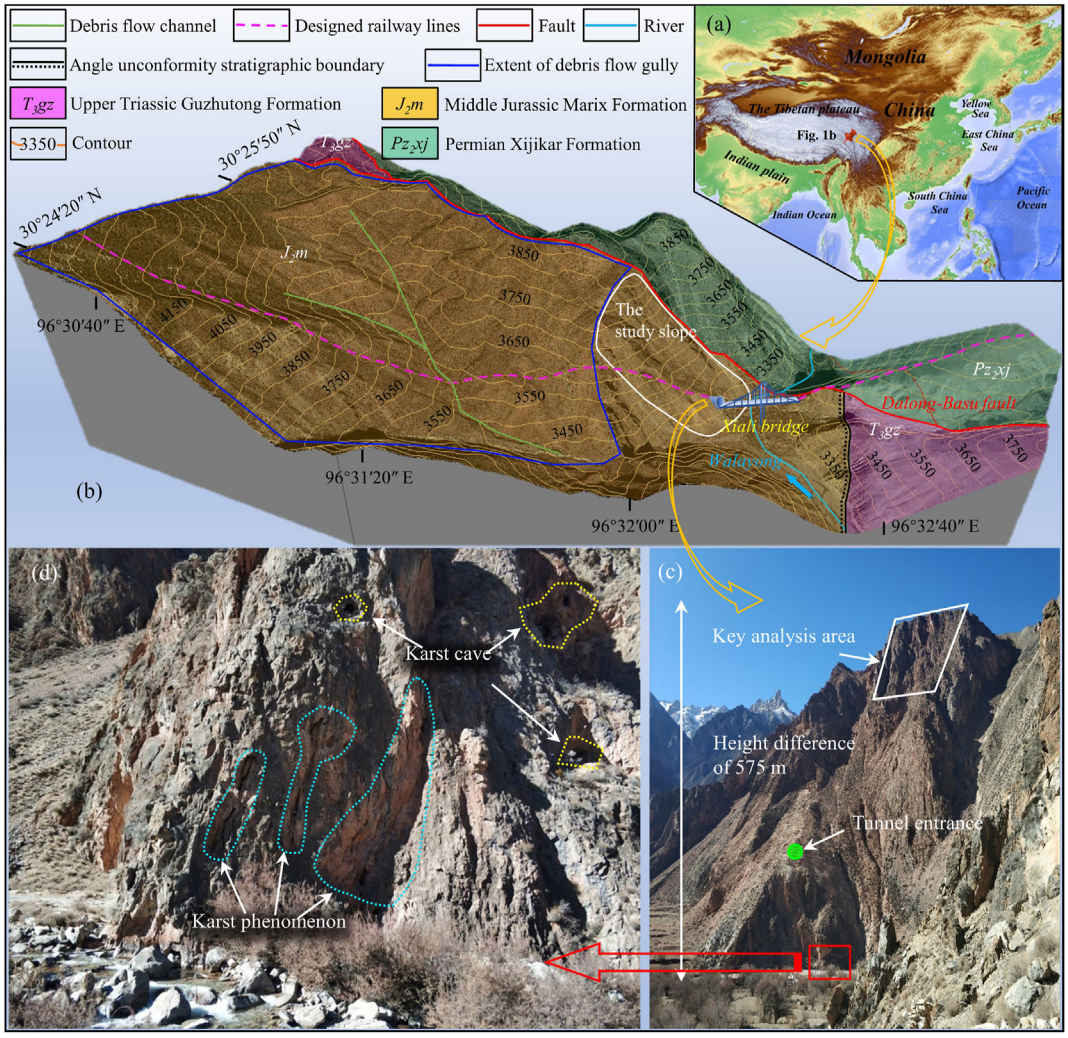

Fig. 1. Geographical location and geological background of the study area: (a) The geographical location of the study area, (b) A 3D geological map of the study area, (c) An overall photo of the slope, and (d) The karst phenomenon developed at the bottom of the slope.

engineering. Thus, the focus of this study is on the collection and analysis of aperture of fractures in rock masses.

3. Methods

3.1. The multi-angle nap-of-the-object photogrammetry

To obtain high-resolution UAV images of high-steep rock slope, a multi-angle nap-of-the-object photogrammetry technique is proposed. The core technology includes four parts: site survey, acquisition of low-resolution 3D terrain in the survey area, multi-angle nap-of-the-object photography strategy design and image acquisition, UAV image quality enhancement and 3D modeling. Fig. 2 shows the key technical steps of multi-angle nap-of-the-object photography.

The initial step involves a site survey to determine the slope morphology of the study area, collect fundamental parameters of the slope and rock structure, and identify the optimal landing site for on-site UAV photography.

The second step involves using oblique photogrammetry supported by terrain-following flight technology to obtain low-resolution 3D terrain data of the study area (Lee et al., 2022; Ren et al., 2022). These data serve as a crucial reference for designing multi-angle nap-of-the-object photogrammetry flight paths.

The third step involves designing a multi-angle nap-of-the-object photogrammetry strategy and acquiring images. The slope terrain and discontinuity features are analyzed using the 3D terrain data from the previous step. This includes measuring the slope height and width, determining the position distribution of key target areas, assessing the dominant orientation of discontinuities. Key target areas include complex raised blocks, reverse slope surfaces and areas prone to occlusion. Next, the position of each flight path is manually set in DJI Terra software based on the required photography distance and the undulating topography of the slope. It is recommended to design the flight paths in an S-shape from the foot to the top of the slope. The design of the photography angles should include both vertical to the slope surface and perpendicular to each set of discontinuities. For key target areas, additional photography angles and image overlap should be appropriately increased to achieve complete coverage.

The number of routes to be designed in the horizontal direction (x) can be calculated according to Eq. (1). Its flight speed in the horizontal and vertical directions (V_h, V_p) needs to be calculated according to Eqs. (2) and (3) (Fig. 5a and c).

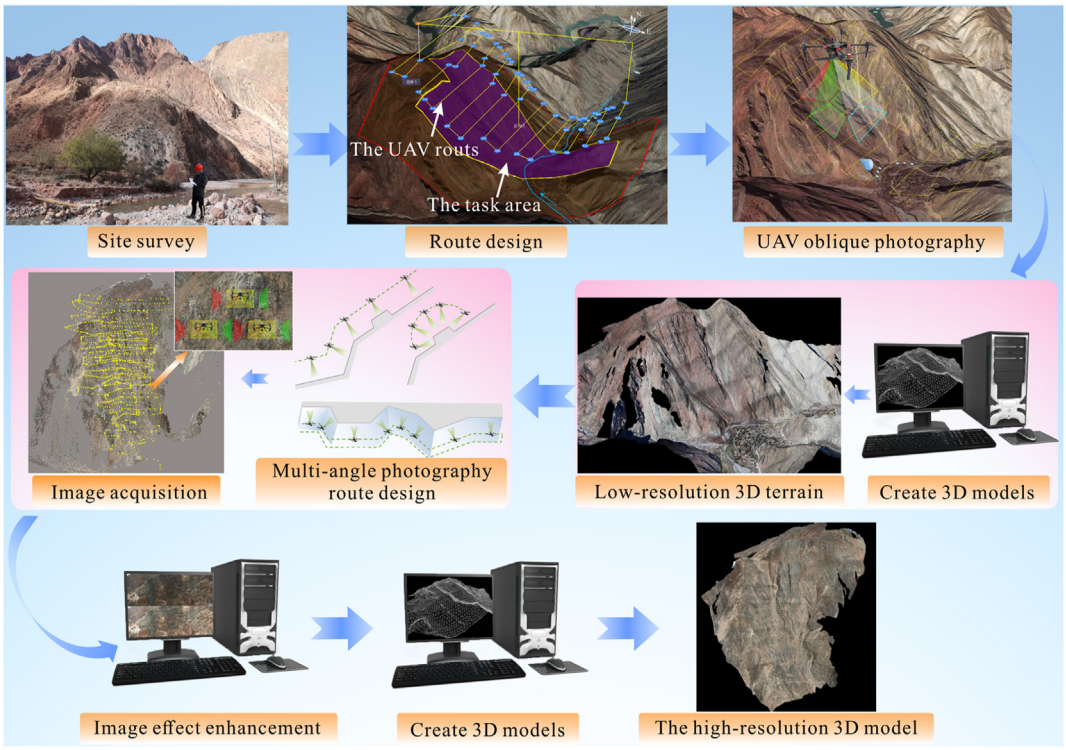

Fig. 2. The technical process of multi-angle nap-of-the-object image acquisition.

$$x = \frac{fH - aDC_h}{aDC_p(1-p)} + 1 \text{ (rounds toward positive infinity)} \quad (1)$$

$$v_h = \frac{aDC_h(1-h)}{tf} \quad (2)$$

$$v_p = \frac{aDC_p(1-p)}{tf} \quad (3)$$

where a is the sensor pixel dimension; f is the focal length of the camera lens, h is the frontal overlap, p is the side overlap, t is the time interval for the UAV to take pictures, H is the slope height, C_h is the number of pixels on the long side of the sensor, C_p is the number of pixels on the short side of the sensor, and D means the photography distance.

To fully exploit the potential of multi-angle nap-of-the-object images, partial image quality enhancement is required prior to 3D modeling. For multiple images with similar scenes and lighting conditions, the FeiMa company's UAV Manger software can use one image as a template to achieve color and brightness consistency by adjusting the color space components of other images to match those of the template image. For a small number of images with different scenes and lighting conditions, the brightness and color characteristics of the images can be manually adjusted using Photoshop software. The goal is to achieve overall color balance within each individual image, minimizing significant differences in brightness. Enhanced images are more effective for identifying and

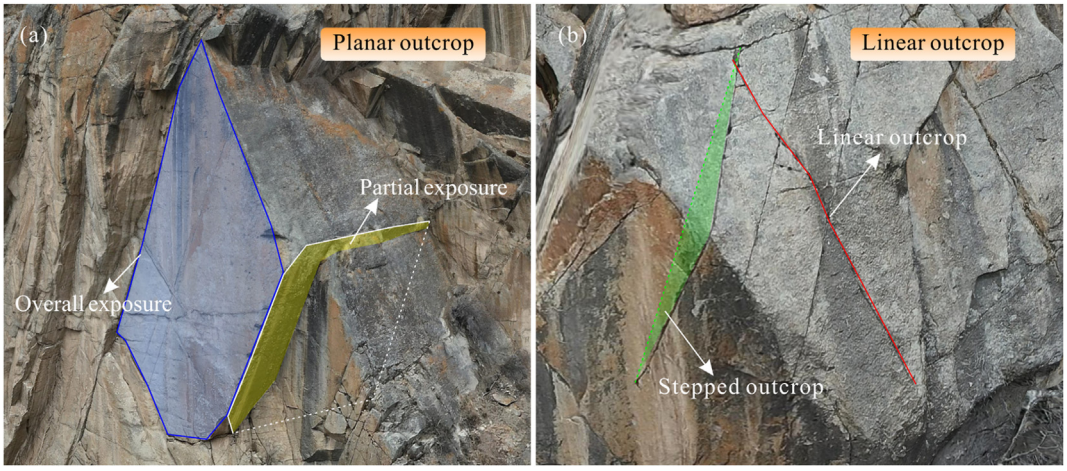

Fig. 3. The outcrop types of rock mass discontinuities and the selection of feature points: (a) Planar outcrop, and (b) Linear outcrop.

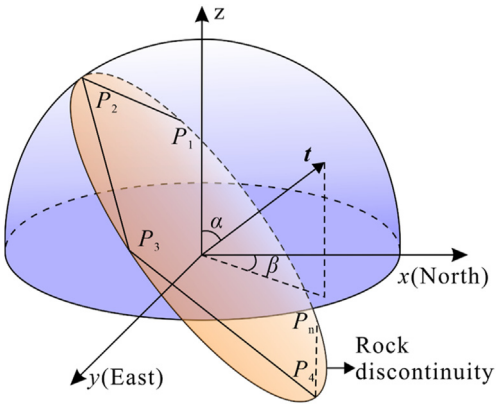

Fig. 4. Representation of the rock discontinuity orientation.

interpreting fracture aperture, according to experimental results. Finally, a high-quality real scene 3D model of the slope is created in OSGB format using DJI Terra software, for use in interpreting rock mass structural parameters.

3.2. Fracture identification and aperture interpretation

3.2.1. Fracture identification and orientation calculation

Based on the basic characteristics of the naturally exposed discontinuities, they can be grouped into two categories. Planar outcrops can be divided into two forms: overall exposure and partial exposure (Fig. 3a). Linear outcrops include linear and stepped types (Fig. 3b).

Theoretically, the discontinuity plane can be characterized by taking 3 non-collinear feature points on the discontinuity. However, when the roughness of the discontinuity is large, the location of the points will seriously affect the characterization results. Therefore, it is recommended to treat the visible exposed area of the discontinuity as an irregular polygon and to take the corner points of its edges as the feature points for measurement. Fig. 4 shows the schematic diagram of the discontinuity orientation interpretation principle.

Suppose that n $(n \geq 3)$ feature points $P_i(x_i, y_i, z_i), (i = 1, 2, \ldots, n)$ are measured on a discontinuity, the equation of the discontinuity can be expressed as $z = Ax + By + C$. Then, the dip direction (β) and the dip (α) of this discontinuity can be solved using the following algorithm (Song et al., 2022):

$$\begin{bmatrix} A \\ B \\ C \end{bmatrix} = \left(\begin{bmatrix} X_1 & Y_1 & 1 \\ X_2 & Y_2 & 1 \\ \vdots & \vdots & \vdots \\ X_n & Y_n & 1 \end{bmatrix}^{\mathrm{T}} \begin{bmatrix} X_1 & Y_1 & 1 \\ X_2 & Y_2 & 1 \\ \vdots & \vdots & \vdots \\ X_n & Y_n & 1 \end{bmatrix} \right)^{-1} \begin{bmatrix} X_1 & Y_1 & 1 \\ X_2 & Y_2 & 1 \\ \vdots & \vdots & \vdots \\ X_n & Y_n & 1 \end{bmatrix}^{\mathrm{T}} \begin{bmatrix} Z_1 \\ Z_2 \\ \vdots \\ Z_n \end{bmatrix} \tag{4}$$

When $A = 0$, we have

$$\left.\begin{aligned} \alpha &= |\arctan(B)| \\ \beta &= \begin{cases} \pi/2 & (B < 0) \\ 3\pi/2 & (B > 0) \\ \forall\,(B = 0) \end{cases} \end{aligned}\right\} \tag{5}$$

When $A \neq 0$, we have

$$\left.\begin{aligned} \alpha &= \left|\arctan\left(\sqrt{A^2 + B^2}\right)\right| \\ \beta &= \begin{cases} \arctan(B/A) & (A < 0, B \leq 0) \\ \arctan(B/A) + 2\pi & (A < 0, B > 0) \\ \arctan(B/A) + \pi & (A > 0) \end{cases} \end{aligned}\right\} \tag{6}$$

For linear outcrops, the principle of orientation solving is the same. When measuring feature points, the stepped outcrop requires measuring corner points at each corner. For linear outcrops, it is sometimes necessary to extend an additional point, within a controlled range, to determine that fracture plane. This requires the surveyor to have knowledge and experience of discontinuity development, otherwise, it will lead to large deviations.

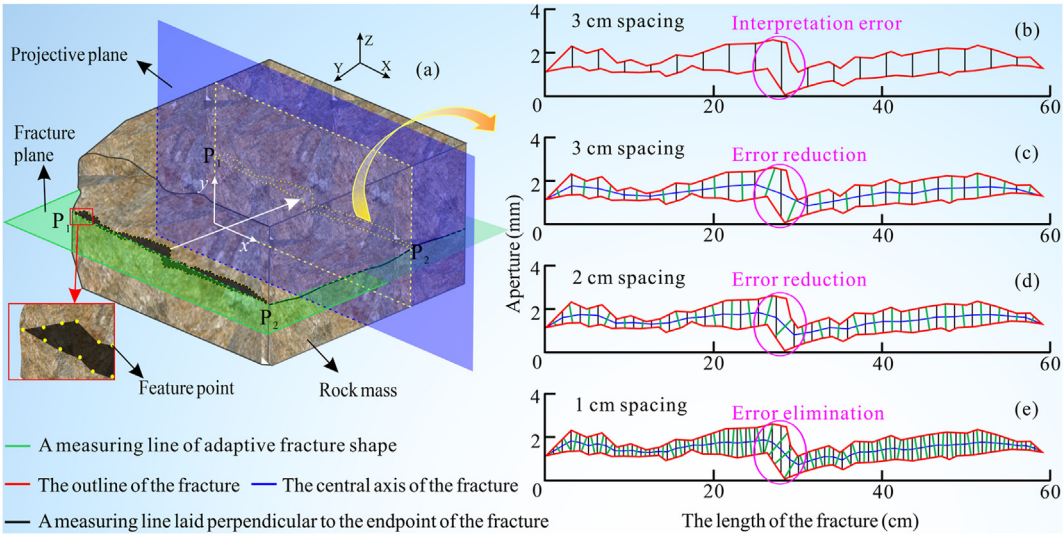

Fig. 5. The principle diagram for aperture interpretation: (a) Measurement and projection of open edge feature points for linear outcrops, (b) The conventional vertical line method, and (c–e) Adaptive fracture shape method with different measuring line spacing.

3.2.2. Aperture interpretation algorithm with adaptive fracture shape

This study focuses on the identification and interpretation of linear fracture apertures. The specific processes are described as follows.

Step 1 is the feature points measurement. On the slope 3D model, measure all vertices of the irregular polygon along the open edge of the fracture (Fig. 5a). To ensure the real shape of a fracture, the edge inflection points should be measured as much as possible.

Step 2 is the Feature points projection. The opening of rock fractures has some undulation and is not a flat ideal state. To accurately interpret the vertical distance between two rock walls, all edge feature points of the fractures need to be projected onto a plane perpendicular to the fracture plane (Fig. 5a).

Firstly, it is necessary to determine the projection plane. Assuming the dip direction of the fracture plane is β, the dip is α, its normal vector can be expressed as $\vec{n} = (l_1, l_2, l_3)$, where $l_1 = \sin\beta\cos\alpha$, $l_2 = \sin\beta\sin\alpha$, $l_3 = \cos\beta$. Assuming that the unit normal vector of the projection plane is $\vec{m}$ (A,B,C), then $A^2 + B^2 + C^2 = 1$, and $\vec{n}\cdot\vec{m} = 0$. To fix the position of the projection plane, let the vertices $P_1(x_1,y_1,z_1)$ and $P_2(x_2,y_2,z_2)$ at the two ends of the fracture be on the projection plane. From the projection plane of P_1 and P_2, and the vectors $\overrightarrow{P_1P_2}$ and $\vec{m}$ are perpendicular to each other, we have $\Delta xA + \Delta yB + \Delta zC = 0$. The normal vector of the projection plane can be obtained by combining the above equations:

$$\left.\begin{aligned} A &= -(l_3y_1 - l_3y_2 - l_2z_1 + l_2z_2)/(l_2x_1 - l_2x_2 - l_1y_1 + l_1y_2) \\ B &= -(-l_3x_1 + l_3x_2 + l_1z_1 - l_1z_2)/(l_2x_1 - l_2x_2 - l_1y_1 + l_1y_2) \\ C &= -(-l_3x_2y_1 + l_3x_1y_2 + l_2x_2z_1 - l_1y_2z_1 - l_2x_1z_2 + l_1y_1z_2)/(l_2x_1 - l_2x_2 - l_1y_1 + l_1y_2) \end{aligned}\right\} \tag{7}$$

Then, all edge feature points of the fractures are projected onto the projection plane. Assuming that the coordinate of the feature point is $P(x_0,y_0,z_0)$, a perpendicular line is drawn from P to the projection plane, resulting in the foot $P_t(x_{t0},y_{t0},z_{t0})$. The P_t is the projected point to be found.

$$\left.\begin{aligned} x_{t0} &= x_0 - Au \\ y_{t0} &= y_0 - Bu \\ z_{t0} &= z_0 + u \end{aligned}\right\} \tag{8}$$

where

$$u = \frac{Ax_0 + By_0 - z_0 + C}{A^2 + B^2 + 1} \tag{9}$$

In Step 3, although the projected feature points are on the same plane, they still represent a mathematical problem in 3D space. To simplify subsequent data processing and facilitate graphical representation, Wang et al. (2020)'s method is introduced for coordinate system transformation. After transformation, the z-coordinate of all feature points becomes 0, simplifying the mathematical problem from 3D space to a 2D plane. In the new coordinate system, the line connecting the two endpoints of the fracture is defined as the x-axis, and the direction perpendicular to x-axis passing through the third point is defined as the y-axis. The specific procedure of coordinate system transformation is as follows:

(1) To achieve a transformation from coordinate system O-XYZ to $P_1 - X''Y''Z$, the two endpoints of the fracture $P_1(x_1,y_1,z_1)$ and $P_2(x_2,y_2,z_2)$, and a non-collinear third point $P_3(x_3,y_3,z_3)$ are selected, and a translation ($O \rightarrow P_1$) and counterclockwise rotation around the z-axis by an angle ε_Z is applied:

$$\begin{pmatrix} X_i'' \\ Y_i'' \\ Z_i \end{pmatrix} = \frac{1}{\lambda}\begin{bmatrix} (X_i - X_1)\cos\varepsilon_Z + (Y_i - Y_1)\sin\varepsilon_Z \\ -(X_i - X_1)\sin\varepsilon_Z + (Y_i - Y_1)\cos\varepsilon_Z \\ Z_i - Z_1 \end{bmatrix} \tag{10}$$

where $1/\lambda$ is the scaling.

When $\Delta X_{21} = 0$, we have

$$\varepsilon_Z = \begin{cases} \pi/2 & (\Delta Y_{21} > 0) \\ 3\pi/2 & (\Delta Y_{21} < 0) \end{cases} \tag{11}$$

When $\Delta X_{21} \neq 0$, we have

$$\varepsilon_Z = \begin{cases} \arctan(\Delta Y_{21}/\Delta X_{21}) & (\Delta X_{21} > 0, \Delta Y_{21} > 0) \\ 2\pi + \arctan(\Delta Y_{21}/\Delta X_{21}) & (\Delta X_{21} > 0, \Delta Y_{21} < 0) \\ \pi + \arctan(\Delta Y_{21}/\Delta X_{21}) & (\Delta X_{21} < 0) \end{cases} \tag{12}$$

(2) A transformation from coordinate system $P_1 - X''Y''Z$ to $P_1 - X'Y''Z''$ is achieved by rotating clockwise around the Y'' axis by an angle ε_Y:

$$\begin{pmatrix} X_i' \\ Y_i'' \\ Z_i'' \end{pmatrix} = \frac{1}{\lambda}\begin{bmatrix} (X_i - X_1)\cos\varepsilon_Z\cos\varepsilon_Y + (Y_i - Y_1)\sin\varepsilon_Z\cos\varepsilon_Y + (Z_i - Z_1)\sin\varepsilon_Y \\ -(X_i - X_1)\sin\varepsilon_Z + (Y_i - Y_1)\cos\varepsilon_Z \\ -(X_i - X_1)\cos\varepsilon_Z\sin\varepsilon_Y - (Y_i - Y_1)\sin\varepsilon_Z\sin\varepsilon_Y + (Z_i - Z_1)\cos\varepsilon_Y \end{bmatrix} \tag{13}$$

where

$$\varepsilon_Y = \begin{cases} \arctan\left[\dfrac{Z_2 - Z_1}{(X_2 - X_1)\cos\varepsilon_Z + (Y_2 - Y_1)\sin\varepsilon_Z}\right] & (\Delta Z_{21} > 0) \\ 2\pi + \arctan\left[\dfrac{Z_2 - Z_1}{(X_2 - X_1)\cos\varepsilon_Z + (Y_2 - Y_1)\sin\varepsilon_Z}\right] & (\Delta Z_{21} < 0) \end{cases} \tag{14}$$

(3) A transformation from coordinate system $P_1 - X'Y''Z''$ to $P_1 - X'Y'Z'$ is achieved by rotating counterclockwise around the X' axis by an angle ε_X:

$$\begin{pmatrix} X_i' \\ Y_i' \\ Z_i' \end{pmatrix} = \frac{1}{\lambda}\begin{pmatrix} 1 & 0 & 0 \\ 0 & \cos\varepsilon_X & \sin\varepsilon_X \\ 0 & -\sin\varepsilon_X & \cos\varepsilon_X \end{pmatrix}\begin{pmatrix} \cos\varepsilon_Y & 0 & \sin\varepsilon_Y \\ 0 & 1 & 0 \\ -\sin\varepsilon_Y & 0 & \cos\varepsilon_Y \end{pmatrix}\begin{pmatrix} \cos\varepsilon_Z & \sin\varepsilon_Z & 0 \\ -\sin\varepsilon_Z & \cos\varepsilon_Z & 0 \\ 0 & 0 & 1 \end{pmatrix}\begin{pmatrix} X_i - X_1 \\ Y_i - Y_1 \\ Z_i - Z_1 \end{pmatrix} \tag{15}$$

When $\Delta Y''_{31} = 0$, we have

$$\varepsilon_X = \begin{cases} \pi/2 & (\Delta Z''_{31} > 0) \\ 3\pi/2 & (\Delta Z''_{31} < 0) \end{cases} \tag{16}$$

When $\Delta Y''_{31} \neq 0$, we have

$$\varepsilon_X = \begin{cases} \arctan(\Delta Z''_{31}/\Delta Y''_{31}) & (\Delta Y''_{31} \text{ and } \Delta Z''_{31} \text{ have the same sign}) \\ 2\pi + \arctan(\Delta Z''_{31}/\Delta Y''_{31}) & (\Delta Y''_{31} \text{ and } \Delta Z''_{31} \text{ have different signs}) \end{cases} \tag{17}$$

where $\Delta Z''_{31} = P'_3P''_3$, $\Delta Y''_{31} = P_1P''_3$.

Step 4 is the determination of aperture under the vertical measuring line. Connecting the feature points at the beginning and the end of the edge of the fracture after coordinate transformation draws the sketch of aperture shape (Fig. 5b). Dividing the fracture edge into upper and lower parts with the end points of the fracture as the boundary, each part can be expressed in the form of a segmented function. Specifying the measuring line spacing k, measuring lines L_1 are laid out in sequence along the positive x-axis direction. Then, the aperture at any position of the fracture is the distance between the intersection points of the measuring line and the upper and lower edges of the fracture. It should be emphasized that this method is only suitable for straight aperture shapes. For fractures with large undulations, large interpretation differences may occur (the purple ellipse in Fig. 5b). In view of this phenomenon, it is necessary to further set up measuring lines adapted to the fracture shape to solve this problem.

Step 5 is the determination of aperture adapted to fracture shape. Extract the midpoints of all the vertical measuring lines in the fourth step and connect them end to end to obtain the central axis of the fracture composed of several line segments (the blue lines in Fig. 5c–e). Then extract the midpoints of each section of the central axis, and make the perpendicular line L_2 of the central axis through this midpoint (the green lines in Fig. 5c–e). At this time, the distance between the measuring line and the intersection points of the fracture edge is the final required aperture.

Assume that the coordinates of the midpoint of the central axis are $M(x_i, y_i)$ $(i = 1, 2, 3, \cdots, n+1)$, the endpoint coordinates of each segment of the central axis are $J(x_i, y_i)$ $(i = 1, 2, 3, \cdots, n+2)$, and the starting and ending coordinates of the fracture are $P_s(x_s, y_s)$ and $P_e(x_e, y_e)$. The coordinates of the intersection point of the measuring line L_2 and the edge line of the upper part of the fracture $P_u(x_{ui}, y_{ui})$ can be calculated according to the following equation:

When $J(y_{i+1}) - J(y_i) = 0$, we have

$$\left.\begin{aligned} x_{ui} &= M(x_i) \\ y_{ui} &= [M(y_i) - x_s]\frac{\Delta y}{\Delta x} + y_s \end{aligned}\right\} \tag{18}$$

When $J(x_{i+1}) - J(x_i) = 0$, we have

$$\left.\begin{aligned} x_{ui} &= [M(y_i) - y_s]\frac{\Delta x}{\Delta y} + x_s \\ y_{ui} &= M(y_i) \end{aligned}\right\} \tag{19}$$

When $J(x_{i+1}) - J(x_i) \neq 0$ and $J(y_{i+1}) - J(y_i) \neq 0$, we have

$$\left.\begin{aligned} x_{ui} &= \left[kM(x_i) - M(y_i) - x_s\frac{\Delta y}{\Delta x} + y_s\right] \Big/ \left(k - \frac{\Delta y}{\Delta x}\right) \\ y_{ui} &= \left[M(y_i) - kM(x_i) - ky_s\frac{\Delta x}{\Delta y} + kx_s\right] \Big/ \left(1 - k\frac{\Delta x}{\Delta y}\right) \end{aligned}\right\} \tag{20}$$

where $k = -\frac{J(x_{i+1}) - J(x_i)}{J(y_{i+1}) - J(y_i)}$, $\Delta x = x_e - x_s$, $\Delta y = y_e - y_s$.

In the same way, the coordinates of the intersection point of the measuring line L_2 and the edge line of the lower part of the fracture $P_l(x_{li}, y_{li})$ can be calculated. Then the aperture d_i $(i = 1, 2, 3, \ldots, n+1)$ at the current position can be expressed as

Table 1
UAV specifications and aerial photography task parameters.

Item	Parameter	Specification (FeiMa D200/ M300RTK)
Aircraft	Net mass (kg)	6.5/6.3
	Max flight time (min)	48/55
	Rate wind speed (m/s)	10/10
	Positioning accuracy	Horizontal 1 cm + 1 ppm/ 1 cm + 1 ppm Vertical 2 cm + 1 ppm/ 1.5 cm + 1 ppm
Camera	Net mass (kg)	1.45/0.8
	Sensor size (mm × mm)	23.5 × 15.6/35.9 × 24
	Pixel dimension (mm)	0.0039/0.0044
	Number of lenses	5/1
	Lens focus (mm)	Vertica camera 25, Tilt camera 35/35
The task parameters	Flight altitude/Photography distance (m)	191/60
	Frontal overlap (%)	80/85
	Side overlap (%)	60/70
	Theoretical ground sampling distance (cm)	3/0.8

$$d_i = \sqrt{(x_{ui} - x_{li})^2 + (y_{ui} - y_{li})^2} \tag{21}$$

Then the maximum aperture d_{imax}, minimum aperture d_{imin}, and average aperture d_{iavg} of the fracture can be calculated.

Based on the aforementioned algorithm, the authors developed an aperture interpretation and analysis software of adaptive fracture shape (AIA). The software provides automated batch calculation, analysis, and graphical representation of the aperture based on the feature points of the fracture edge.

3.3. Aperture probability distribution test

In the study, the Kolmogorov-Smirnov (K–S) test method is used to test the probability distribution form of the fracture aperture. The main idea of the method is as follows.

For a certain sample with n observations, a step-like cumulative frequency function can be constructed by sorting them from smallest to largest (Schellhaas, 1999):

$$S_n(x) = \begin{cases} 0 & (x < x_1) \\ k/n & (x_k \le x < x_{k+1}) \\ 1 & (x \ge x_n) \end{cases} \tag{22}$$

where $x_1, x_2, \ldots, x_n$ are the sorted sample values.

Table 2
A comparison of the orientation obtained by the two methods.

No.	3D model-based measurement		Field survey		Difference	
	Dip direction (°)	Dip (°)	Dip direction (°)	Dip (°)	Dip direction (°)	Dip (°)
1	166	89	166	89	0	0
2	279	68	281	67	−2	1
3	35	68	35	69	0	−1
4	266	69	270	69	−4	0
5	104	70	105	70	−1	0
…	…	…	…	…	…	…
54	236	63	238	64	−2	−1

Table 3
A comparison of the trace length and aperture obtained by the two methods.

No.	3D model-based measurement		Field survey		Difference	
	Trace length (m)	Aperture (cm)	Trace length (m)	Aperture (cm)	Trace length (m)	Aperture (cm)
1	6.624	1.9	6.641	0.8	−1.7	1.1
2	8.423	0.7	8.435	1.7	−1.2	−1.0
3	28.321	2.2	28.328	2.2	−0.7	0.0
4	12.261	0.6	12.269	0.4	−0.8	0.2
5	4.563	0.7	4.582	1.5	−1.9	−0.8
…	…	…	…	…	…	…
25	12.464	0.6	12.459	0.3	0.5	0.3

Table 4
Results of discontinuity grouping in the study area.

Set	Dip direction (°)	Dip (°)	Number of discontinuities	
			All data	For aperture
1	125	76	228	33
2	3	87	275	43
3	291	13	159	49
4	50	66	355	118

In the K–S test, the maximum difference between S_n and the theoretical distribution function F_n over the entire test range (D_n) is the measure of the difference between the theoretical model and the observed data:

$$D_n = \max|F(x) - S_n(x)| \tag{23}$$

Theoretically, D_n is a random variable whose distribution depends on the size of n. For a specific confidence level α, the K–S test

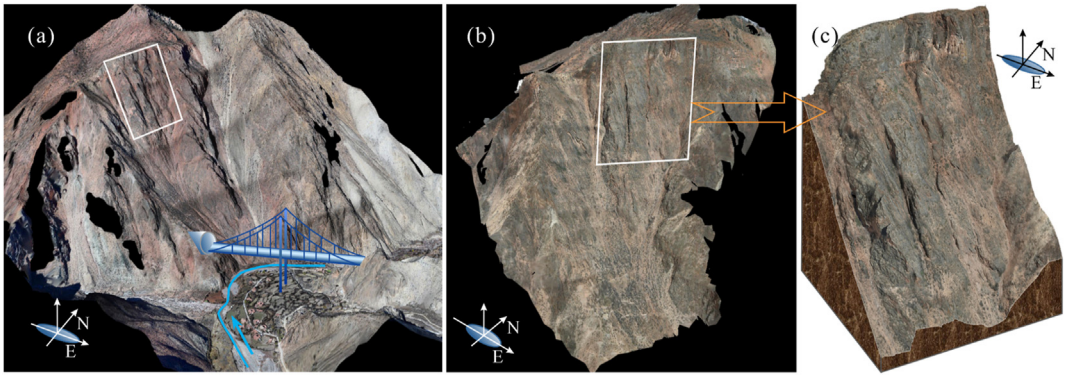

Fig. 6. The 3D models of the study area: (a) The oblique 3D model, (b) The multi-angle nap-of-the-object 3D model, and (c) The key analysis area.

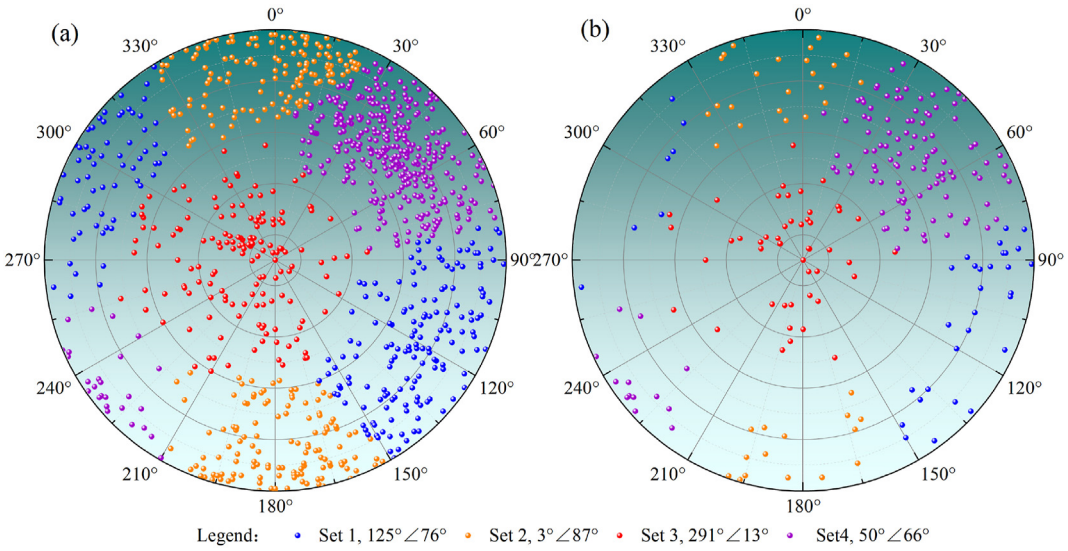

Fig. 7. Discontinuity orientation data visualization: (a) Overall 1017 discontinuities, and (b) 243 fractures for interpreting aperture.

compares the maximum value observed in $D_n = \max|F(x) - S_n(x)|$ with the critical value D_n^{α} (Schellhaas, 1999; Zhang et al., 2010):

$$P(D_n \le D_n^{\alpha}) = 1 - \alpha \tag{24}$$

If $D_n < D_n^{\alpha}$, then the hypothetical distribution is acceptable at that confidence level, otherwise the hypothetical distribution will be rejected.

When there is a situation where several different hypotheses are accepted at the same time, it is necessary to determine a maximum level of acceptance that is consistent with the hypothesis of the original distribution. By the goodness-of-fit test method, the one with a large probabilistic fit (φ) is selected as the optimal form of the distribution:

$$\varphi = 1 - \frac{D_n}{D_n^{\alpha}} \tag{25}$$

According to practical experience and existing research results, a certain parameter of the rock structure may obey a limited number of distribution forms (Priest and Hudson, 1976, 1981), for example, normal, log-normal, gamma and exponential distributions (Wu, 1993; Jiang et al., 2021). In addition to the above four distribution forms, the more common uniform, Poisson, and Rayleigh distributions are added to the test analysis in this study. Although there are many distribution forms of data, this study does not analyze other distribution forms.

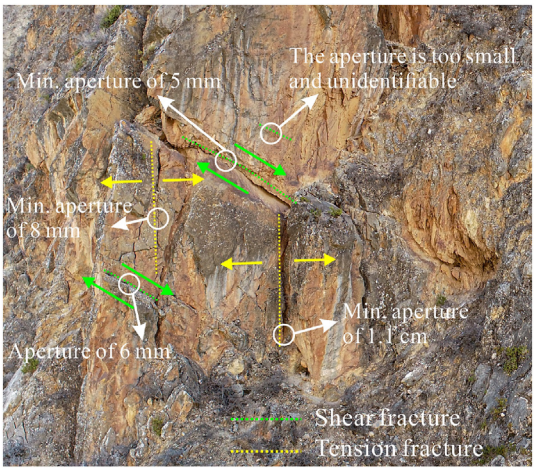

Fig. 8. Interpretable scales of the 3D model.

4. Data acquisition

In this study, a FeiMa D200 UAV with a 5-lens oblique photography module is used to acquire oblique UAV images of the study area by terrain-following flight. The UAV specifications and aerial photography task parameters are shown in Table 1. The aerial photography task takes about 30 min in total, and a total of 1355 images are acquired. Fig. 6a shows the low-resolution 3D model of the survey area. Based on the above results, multi-angle nap-of-the-object photography of the slope of the study area is carried out by using DJI M300 RTK UAV with a P1 camera. The specifications of the UAV and the aerial photography task are shown in Table 1. The aerial photography task takes about 108 min in total and 2277 images are acquired. Fig. 6b shows the high-resolution 3D model of the studied slope.

Both of the above-mentioned UAVs are equipped with GPS positioning systems and integrated with RTK modules to provide real-time centimeter-level positioning data. This ensures that image metadata with centimeter-level absolute positioning accuracy, as well as live 3D models, can be obtained with little or no ground control points applied (Liu et al., 2019; Kersten et al., 2022).

A total of 1017 discontinuities are collected within the key analysis area of the slope, including 243 linear discontinuities. Using the AIA software developed in this study, the aperture of these 243 linear discontinuities is interpreted and analyzed. To verify the accuracy of the discontinuity parameters interpreted based on the 3D model, they are compared with the results of on-site manual investigation. The results show that the maximum difference of the discontinuity dip direction between the two methods is 9°, with an average of 2°; the maximum difference of dip is 5°, with an average of 2° (Table 2); the maximum difference of trace length is 2.6 cm, with an average of 1.3 cm; the maximum difference of aperture is 1.7 cm, with an average of 9 mm (Table 3). The interpretation differences of these parameters meet the engineering requirements.

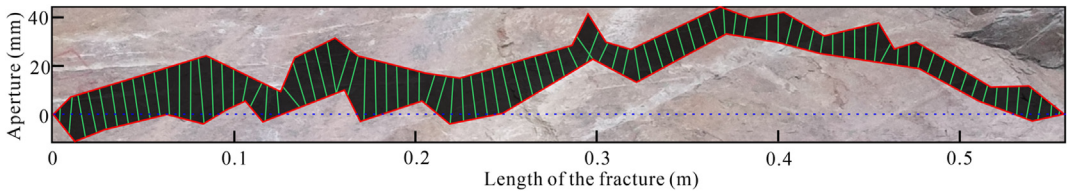

Fig. 9. Morphological diagram of fracture No. Jt-01 (the ratio of the measuring line spacing to the fracture length is r=1%).

The QPSO optimized C-means algorithm (Song et al., 2017) is used to group the discontinuity sets for the study area (Table 4). The orientation pole diagrams of 1017 discontinuities and 243 fractures are given in Fig. 7.

From the grouping results, the first set of discontinuities is outward steeply sloping. The second and fourth sets both steeply dip and intersect the slope at a large angle. The third set is within the gently dipping inside. From the cutting relationship between the discontinuity of each set and the slope (112°∠51°), it will not form a potential block that slides outward to the slope. The third group of discontinuities exhibits a steep dip and runs nearly parallel to the free face. Additionally, examination of the 3D model reveals that many blocks display varying degrees of opening along their trailing edges. Consequently, potential geohazards such as toppling deformation exist within the study area.

5. Results and discussion

5.1. Interpretability of the high-resolution 3D model

The accuracy of identifying and interpreting fracture aperture in a high-steep slope is dependent on the resolution of the 3D model. To verify the interpretability of the 3D model, a selection of fractures are randomly chosen from the high-resolution 3D model of the slope.

As shown in Fig. 8, the minimum aperture that can be directly identified for shear fractures is approximately 5 mm, and smaller apertures cannot be directly identified. For tensile fractures, the minimum aperture that can be directly identified is about 8 mm. Fractures with apertures less than 1 mm, known as “closed” fractures, have little effect on shear strength unless the fracture surface is very smooth. However, the presence of water can significantly alter this situation. In the unloaded zone above the tunnel entrance, particularly at the top of the slope, the aperture scale is typically above millimeter level. Therefore, the resolution of the slope 3D model produced in this study is capable of meeting the interpretation requirements for millimeter-scale fracture apertures. However, the method is currently unable to identify submillimeter openings.

5.2. Interval effect of the aperture

The aperture interpretation algorithm proposed in Section 3.2 is used to interpret the fracture aperture. The distribution form of the aperture is tested at the significance level $\alpha = 0.05$ by using the K–S test. It is found that the maximum and the average aperture of the fracture are different when setting different measuring line spacings, and the distribution form of the aperture is not exactly the same.

The fracture numbered Jt-01 is taken as an example for discussion. Its length is 0.557 m, the orientation is 10°∠81°, and the morphology of the fracture is shown in Fig. 9. The maximum, average and distribution form of the aperture under different measuring line spacings are solved in 1 mm increments, respectively. To ensure that the obtained aperture samples are statistically significant, the number of samples obtained during the aperture interpretation is more than 25, thus only the interpretation results with the measuring line spacing of 23 mm are counted.

There is no doubt that the shape of the fracture opening is varied. Because of this, under different measuring line spacings, there may be situations where the aperture of certain positions cannot be accurately identified and interpreted (Fig. 10). In this way, the maximum aperture of the interpreted fracture and its actual maximum aperture will exist in a certain difference (w). This means that there is a significant interval effect of fracture aperture. This affects the results of the probability distribution test for fracture aperture. It can be seen from Fig. 5c–e that with the decrease of the measuring line spacing, the adaptability of the measuring line to the fracture shape and the ability to correct the difference w are gradually enhanced. Therefore, in this study, the maximum aperture interpreted when the measuring line spacing is 1 mm is taken as the actual maximum aperture value.

The statistical results indicate that as the measuring line spacing increases, the difference w also gradually increases. The maximum difference occurs when the measuring line spacing is 20 mm, with a value of 4.81 mm. The interval effect of fracture aperture has little impact on the average aperture obtained through interpretation. The results show that the average aperture is the smallest (13.59 mm) at a spacing of 14 mm, and the largest (14.08 mm) at a spacing of 18 mm, with a difference of only 0.49 mm between the two.

Although the actual maximum aperture can be obtained at 1 mm spacing, the apertures do not obey the common 7 probability distribution forms for a large number of fractures. In addition, the measurement difference in Fig. 5b is actually a reflection of the interval effect of the aperture. This situation is better avoided by the aperture interpretation algorithm with adaptive fracture shape proposed in this study.

5.3. Optimal sampling length and optimal measuring line spacing for aperture interpreting

In order to determine the most optimal sampling length and corresponding measuring line spacing, 34 fractures are randomly measured in this study. The length range of the fractures is approximately 0.2–1.7 m, and is roughly divided into three length intervals: less than 0.5 m, 0.5–1 m, and 1–2 m. To analyze the reliability of the interpreted results, the aperture is interpreted and the difference w is counted. Due to the inconsistent lengths of the fractures, the ratio (r) of the measuring line spacing to the fracture length is used to characterize the measuring line spacing for convenience of description. To ensure that the number of interpreted aperture samples is statistically significant, the sample size should be greater than 25, corresponding to an r-value of approximately 3%. Therefore, at the data interpretation and statistics stage, all fractures are counted up to $r = 3\%$.

For fractures with a length less of than 0.5 m, it is not difficult to find that there are no data at many locations in Table A1 (Appendix

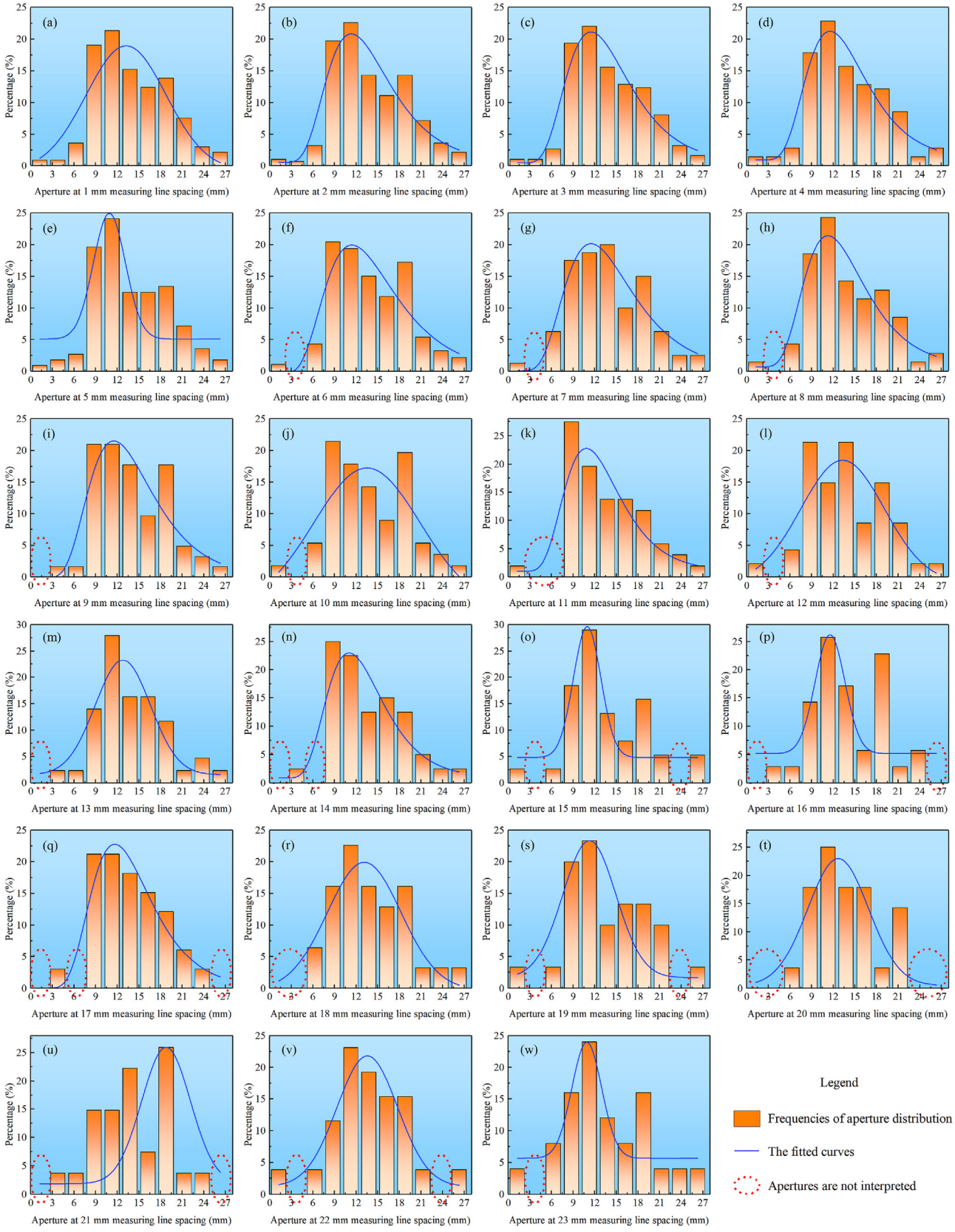

Fig. 10. Histogram of aperture frequency obtained for Jt-01 fracture at different measuring line spacings.

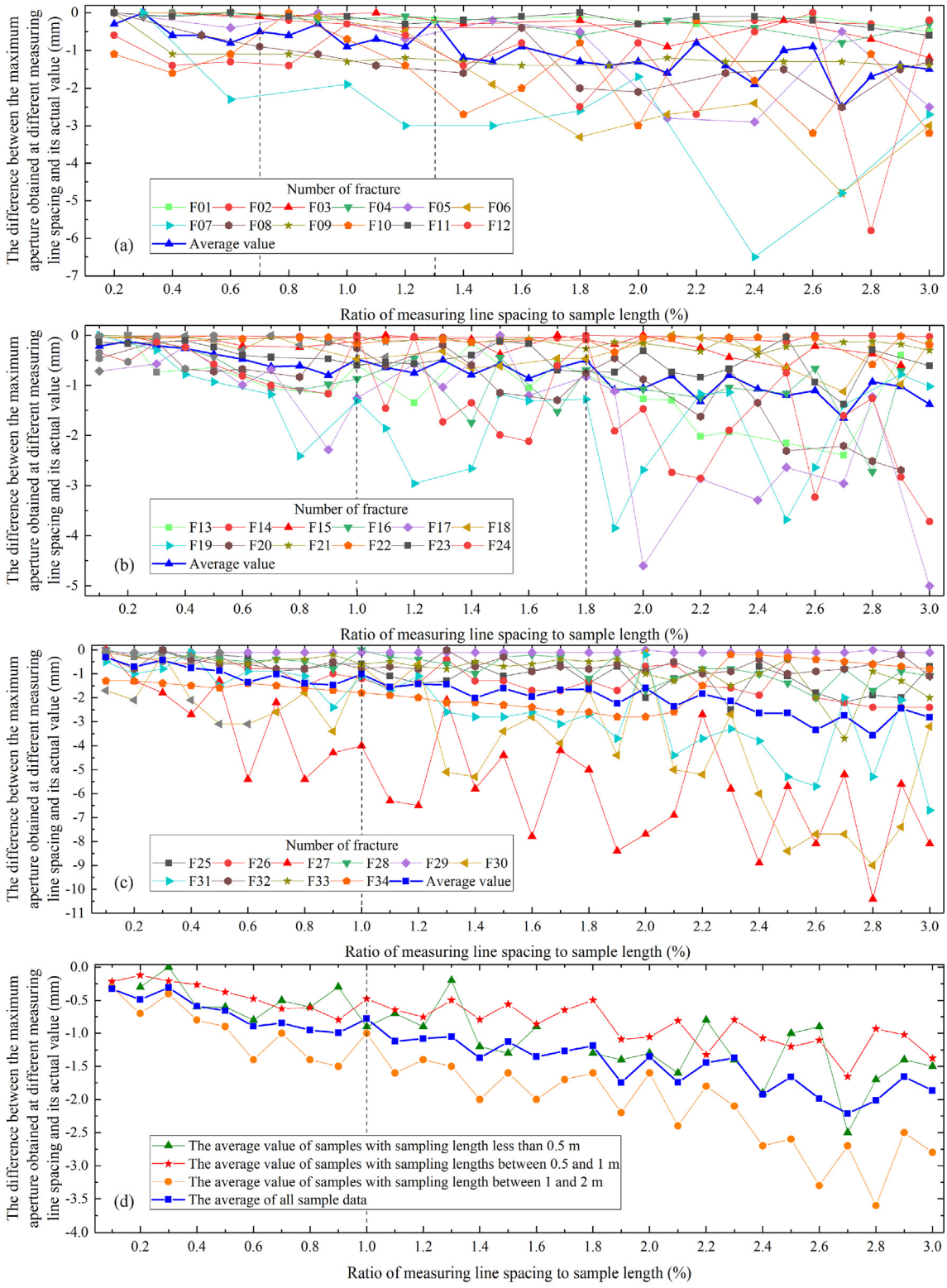

Fig. 11. The difference of the acquired maximum aperture in different measuring line spacings.

A). This is due to the limitation of the length of the fracture itself, which makes it impossible to obtain the aperture samples under some *r*. There are also a few cases where the apertures do not obey the 7 mentioned distribution forms in the study. It is obvious that the value of *w* increases gradually with the increase of the measuring line spacing (Fig. 11). This is because the fracture morphology is complex and the location of the measured fractures varies at different measuring line spacings, which results in the phenomenon that there is always a fracture aperture somewhere that is not measured. Ideally, the aperture obtained at a certain line

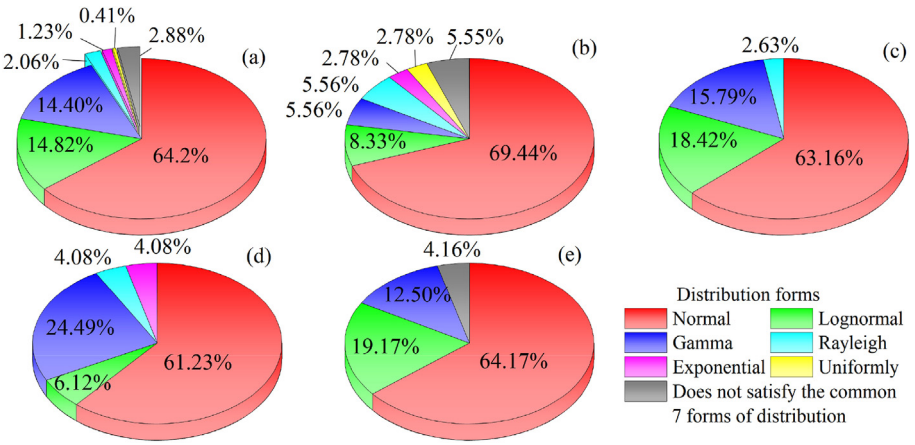

Fig. 12. The pie chart of distribution form for fracture aperture: (a) All 243 fractures, (b) Set 1, (c) Set 2, (d) Set 3, and (e) Set 4.

spacing has a reasonable probability distribution, while the difference w can be controlled to a minimum. When the ratio r is between 0.7% and 1.3%, the difference w is smaller and less fluctuating, basically stable within 1.5 mm, and the average value of difference w is less than 1 mm (Fig. 11a).

It can be seen in Table A2 (Appendix A) that the number of locations without data in the table is significantly reduced compared to fractures with a sampling length of less than 0.5 m. This shows that with the increase of sampling length, the number of cases where interpretation results cannot be obtained under certain r decreases. This is a manifestation of the size effect of fracture aperture. It can be observed that fractures with apertures not following the above 7 common distribution forms still exist when r is less than 1%. In addition, there is a tendency for the w value to gradually increase with the increase of the measuring line spacing (Fig. 11b). On the whole, when the ratio r is between 1% and 1.8%, the difference w is smaller and less fluctuating, basically stable within 2 mm, and the average value of the difference is less than 1 mm. The overall results are more satisfactory.

It is not difficult to find from Table A3 (Appendix A) that there is no data missing. This further reflects the size effect of fracture aperture: with the further increase of sampling length, a statistically significant number of aperture samples can be obtained under any r (take 0%–3%). The cases in which the apertures do not obey the 7 common forms of distribution mentioned above have also been reduced. The w-value still increases gradually with the increase of the measuring line spacing (Fig. 11c). Overall, when the ratio r is about 1%, the difference w is smaller and less fluctuating, basically stable within 2 mm, and the average value of the difference is less than 1 mm. The overall results are more satisfactory.

The above study shows that the fracture aperture has a significant size effect, i.e. the sampling length affects the interpretation results of the aperture. The difference w of the overall interpreting results is the largest when the fracture length is between 1 m and 2 m, and the overall difference w is the smallest when the fracture length is between 0.5 m and 1 m (Fig. 11d). Meanwhile, it is not difficult to conclude that the difference w increases with the increase of the measuring line spacing. Therefore, we conclude that when the fracture length is between 0.5 m and 1 m, it is more reliable to use the proposed fracture width interpreting method to obtain the fracture aperture. To make the interpreting result more ideal, i.e. the aperture has a reasonable probability distribution, and the difference w can be controlled to the minimum, the measuring line spacing should be about 1% of the fracture length.

5.4. Probability distribution of fracture aperture

Overall, 64.2% of the 243 fractures have apertures that follow a normal distribution (Fig. 12 a). This is followed by the log-normal (14.82%) and gamma (14.4%) distributions. Only less than 4% of the fractures have their apertures obeying the Rayleigh, exponential and uniform distributions. There is no fracture whose aperture follows Poisson distribution. Another 2.88% of the fractures do not obey the 7 common forms of distributions counted in the study at r=1%. Fig. 12a indicates that the fracture aperture mostly (over 60%) follows a normal distribution, followed by lognormal (14.82%) and gamma (14.4%) distributions. However, there are certain differences in the distribution of fracture aperture among different fracture sets. For instance, all six common distribution types appear in the first set, while only three common distribution types are observed in the fourth set.

Fractures in set 1 are all outside the steeply dipping slope. In terms of mechanical causes, these are mainly tensile fractures. Because of this, the apertures of this set are the largest (Table 5). Test results show that all six distribution forms are present except the Poisson distribution (Figs. 12b), and 5.56% of the fractures do not obey the common 7 distributions at r=1%. Thus, it can be seen that for tensile fractures, the apertures of single fractures show diversity in the distribution forms. In addition, the maximum and average apertures of this set are taken as data samples respectively to examine the distribution forms of the overall data of tensile fractures. The results show that the maximum and average apertures of the tensile fractures as a whole obeyed log-normal distribution (Table 5).

Fractures in Set 3 are within the gently dipping slope. In terms of mechanical causes, these are mainly shear fractures. Because of this, the apertures of this set are the smallest (Table 5). Test results show that all distribution forms are present except for uniform distribution (Fig. 12d). It can be seen that for shear fractures, the apertures of single fractures also show diversity in the form of distribution. The maximum and average apertures of the shear fractures as a whole obey the gamma distribution (Table 5).

The mechanical causes of fractures in Sets 2 and 4 are more complicated to classify simply. However, their dips are steeper, their dip directions are different by about 130°, and they intersect the slope at a large angle, thus they will be discussed as one type in this study. Overall, the apertures of these two sets are between the 1st and 3rd sets. The test results show that the distribution forms of apertures of these 2 sets are basically normal, log-normal and

Table 5
Aperture statistics of each set of fractures.

Set	Dip direction (°)	Dip (°)	Mean of maximum aperture		Mean of average aperture	
			Aperture (mm)	Distribution	Aperture (mm)	Distribution
1	125	76	44.16	Lognormal	20.91	Lognormal
2	3	87	38.08	Gamma	19.63	Gamma
3	291	13	31.71	Gamma	17.11	Gamma
4	50	66	35	Normal	19.36	Normal

gamma distributions (Fig. 12c and e). Among them, 2.63% of the apertures in Set 2 obey Rayleigh distribution, and the other distribution forms are not present. It can be seen that the apertures of single fractures in these two sets have a strong similarity in the distribution forms, and both show concentration. The maximum and average apertures of all the fractures in Set 2 obeyed the gamma distribution, and all the fractures in Set 4 obeyed the lognormal distribution (Table 5).

5.5. Relationship between fracture aperture and slope altitude

The collected fractures are uniformly distributed within the studied slope (Fig. 13b). Their altitude lies between 3595 m and 3860 m above sea level. Sample data are not collected in some areas on the slope due to the slope deposit covering (Fig. 13b and d). The maximum aperture as well as the average aperture of the 243 fractures on the slope tend to increase with the increase of the slope height (Fig. 13a, c and f). However, the trend of maximum aperture with height is slightly larger than that of average aperture. Unsurprisingly, even at a lower altitude, there are still some tensile fractures with large apertures (Fig. 13e).

From the different dominant sets, there is a trend that the aperture of each set of fractures increases with the slope altitude, and the trend of maximum aperture with height is slightly larger than that of average aperture. The 1st set is the tensile fracture with a steep dip angle and inclination out of the slope, and the aperture is generally larger (Fig. 14a and b). However, the sample size of this set is small because the fracture surface is approximately parallel to the slope surface and not easy to identify and measure. The 3rd set is a gentle dip angle, and the overall aperture diameter is smaller than the other sets (Fig. 14e and f). In contrast, the 2nd and the 4th sets are similar in that both are steeply dipping and intersect the slope at a large angle (Fig. 14c and g). Therefore, the aperture size and its change trend are also similar for the two sets of fractures (Fig. 14d and h).

The multi-phase development of the debris flow gully on the west side of the slope is accompanied by the accompanying gently dipping fractures (Fig. 1b). This is also the main cause of the fractures of Set 3 gently dipping inside the studied slope. The slope becomes gradually steeper during the different phases of river valley downcutting. Meanwhile, the slope unloading effect is always greater at the top than at the bottom, which causes the gently dipping fractures in the study area to show a trend of "steeper at the top and gently at the bottom" with the slope height. Moreover, the

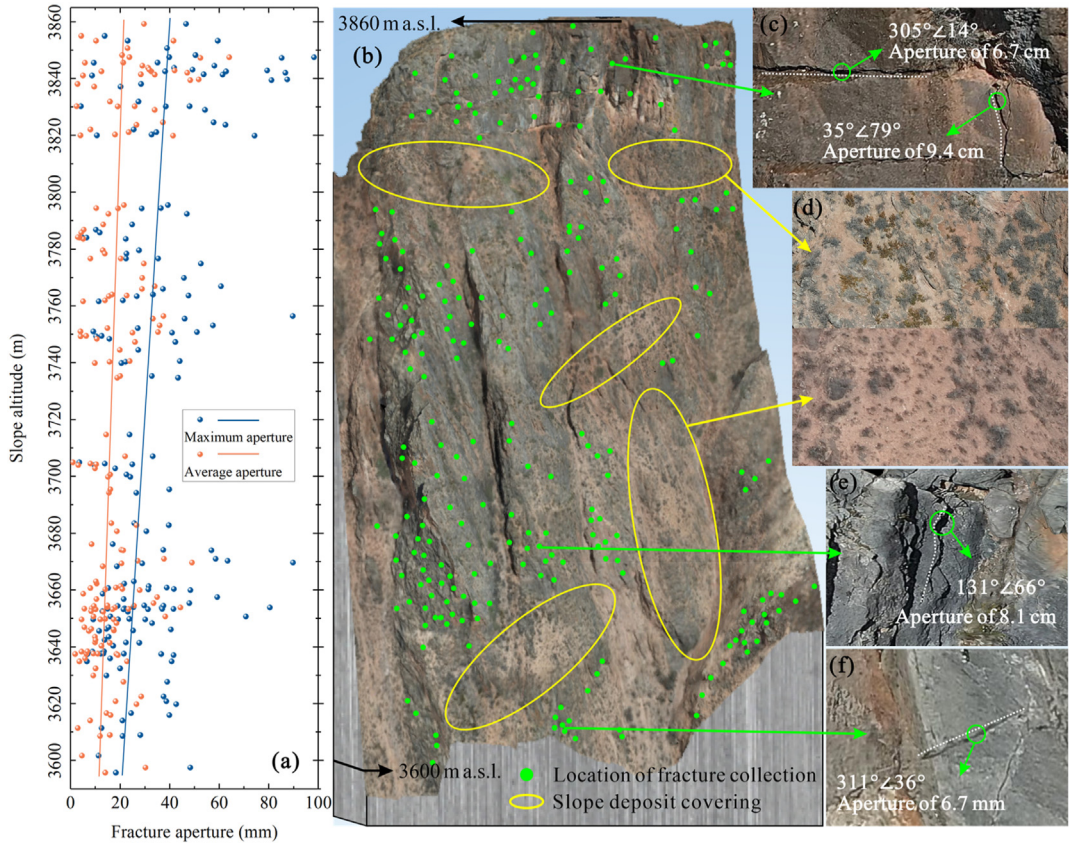

Fig. 13. Schematic diagram of fracture aperture versus slope altitude: (a) Scatter plot of fracture aperture versus slope altitude, (b) Distribution of fracture sampling locations, (c, f) Larger aperture at higher locations and smaller aperture at lower locations, (d) Slope deposit covering, and (e) Larger aperture case at lower locations.

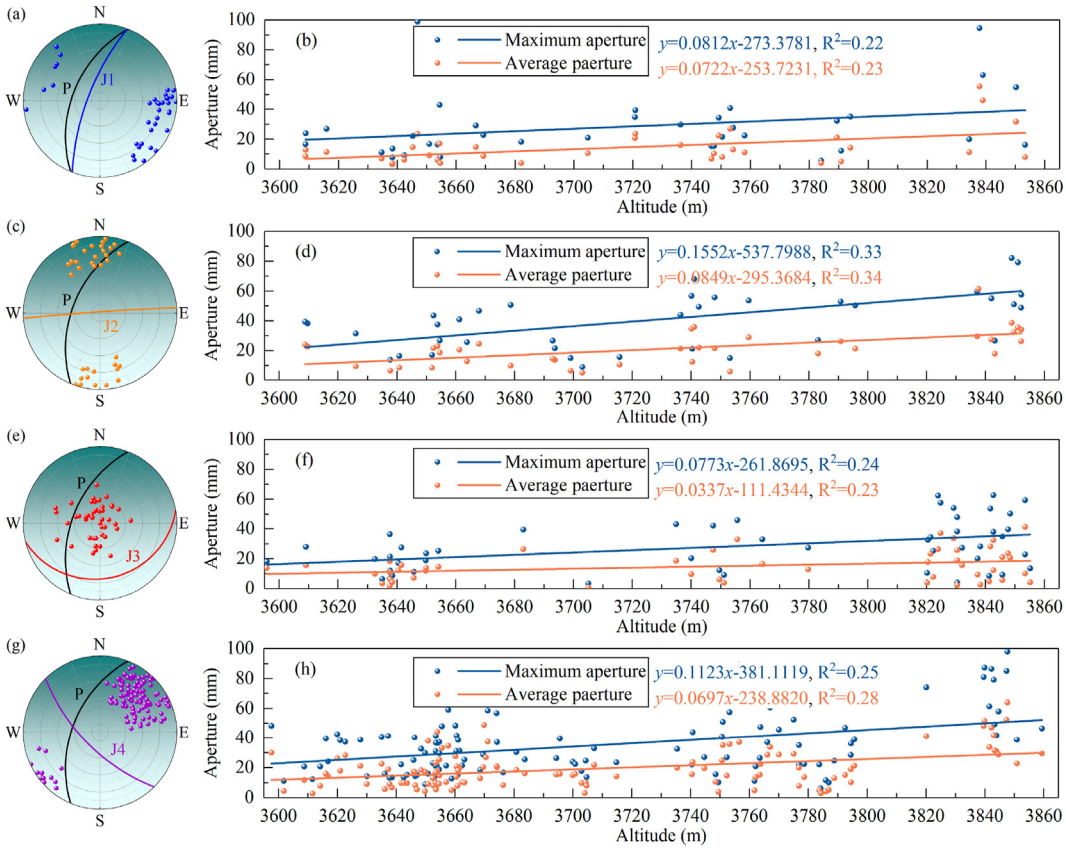

Fig. 14. Analytical plots of fracture aperture with slope altitude for different sets: (a, c, e, g) Upper hemisphere projections of fracture orientation, fracture surface (J_i, i = 1, 2, 3, 4) and slope surface (P) for Sets 1–4, and (b, d, f, h) Scatter plots of fracture aperture with slope altitude for Sets 1–4.

top of the slope is exposed earlier than the bottom, and experiences longer and stronger weathering. This makes the apertures of rock fractures at the top of the slope generally larger than that at the bottom. In addition, the vertical load on the bottom of the slope is greater than that on the top. This makes the aperture of the gently dipping fracture vary more obviously with the change of slope height. Of course, this trend is generally small.

5.6. Relationship between fracture aperture and trace length

From Fig. 15, a positive correlation between fracture aperture and trace length can be observed overall. However, differences exist when examining each set. For example, fractures in Set 1 are mostly tensile fractures, and their trace lengths are generally shorter than those of the other three sets. The trend of increasing fracture aperture with increasing trace length is also most significant in this set. The fractures in Set 3 are formed by shear, with generally longer trace lengths but smaller apertures. The data show that the aperture of shear fractures does not change significantly with the variation of trace length. For the other two sets of fractures, the trace length is comparable, and the trend of aperture change with trace length is roughly similar.

5.7. Applicability and limitations

The multi-angle nap-of-the-object photography technique proposed in this study enables non-contact interpretation of fine parameters of complex rock structures on high-steep slopes. Additionally, the aperture interpretation method of adaptive fracture shape has strong adaptability to linear discontinuities with varying opening shapes. However, there is still room for improvement in this method.

As the constructed 3D model of the slope is a surface model, it can only identify fractures that are exposed on the surface of the rock. Furthermore, the interpretation of aperture for planar discontinuities still poses challenges. Although UAVs are commonly used in surface rock engineering, it does not mean that the aperture interpretation method of adaptive fracture shape is only applicable to outdoor rock structures. If a 3D model of an underground tunnel is established using digital close-range photogrammetry, the proposed interpretation method can still be effective.

Currently, the interpretation method for aperture proposed in this study is mainly constrained by the resolution of the 3D model of the slope. The resolution of the 3D model, in turn, depends on the quality of the UAV image. Therefore, further improvement of the photography technique and enhancement of the UAV image resolution and visual effects will be the focus of future research.

6. Conclusions

The innovation of the study is to propose a new method for rock fracture identification and aperture interpretation based on UAV multi-angle nap-of-the-object images, taking the high-steep rock slope on the left bank of Xiali Station as the study area. The main research results are as follows:

(1) The UAV multi-angle nap-of-the-object photogrammetry is capable of adapting to complex terrain, such as high-steep rock slopes, and provides millimeter-level image resolution. The aperture interpretation algorithm with adaptive fracture

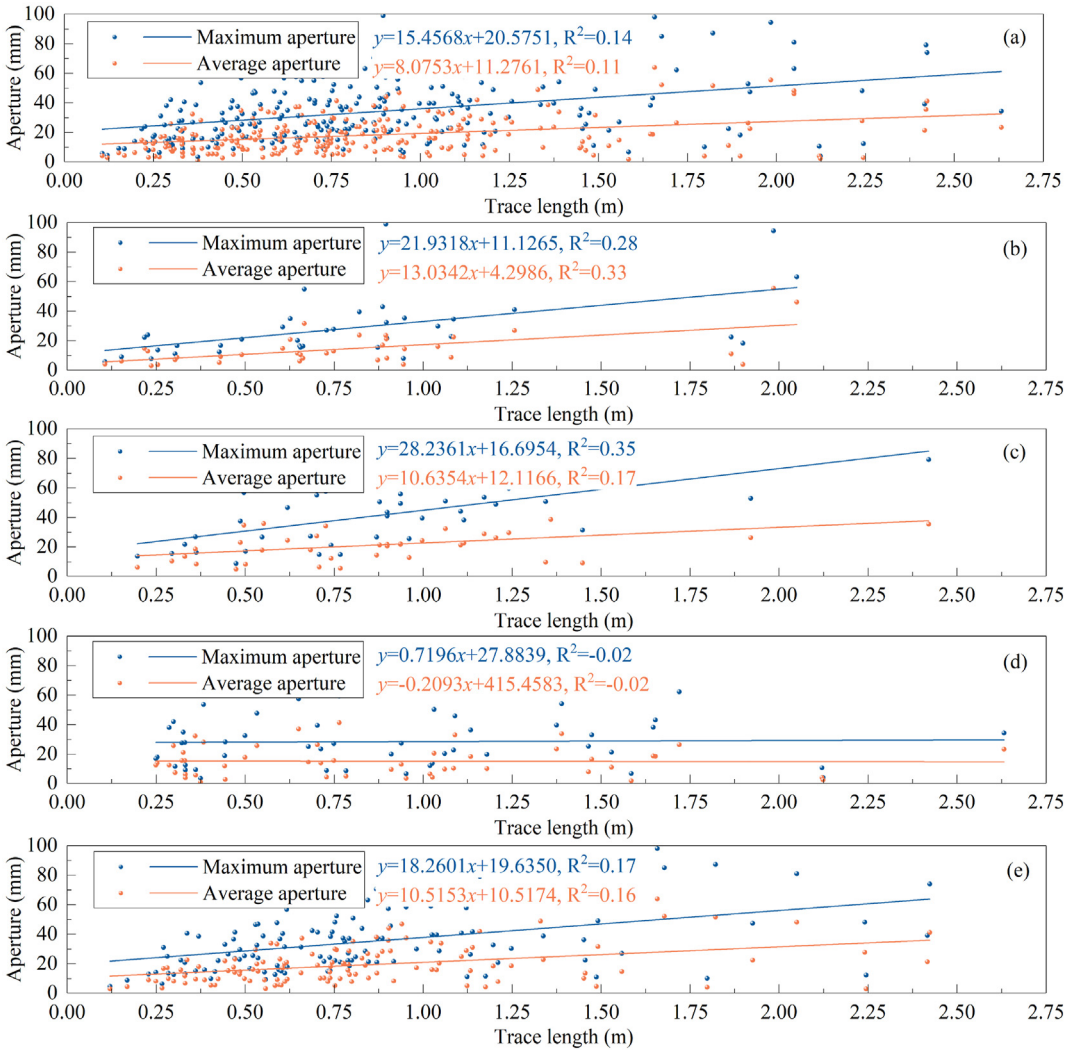

Fig. 15. Relationship between aperture and trace length of fractures in different groups: (a) All 243 fractures, (b) Set 1, (c) Set 2, (d) Set 3, and (e) Set 4.

shape can effectively avoid measurement differences caused by the interval effect and size effect by determining the fracture central axis. This allows for fast and accurate acquisition of millimeter-level fracture aperture information, providing important technical support for fine data collection in rock engineering for safer and cleaner production.

(2) The size effect of fracture aperture can affect the accuracy of its interpretation at different sampling lengths, while the interval effect of aperture can affect the comprehensiveness and accuracy of the apertures obtained at different measuring line spacings. In measuring the morphology feature points of fractures, it is recommended to use a sampling length of 0.5–1 m. When the ratio of measuring line spacing to sampling length is about 1%, the aperture interpretation effect is most satisfactory.

(3) The results of this study indicate that among the fracture sets in the study area, both the maximum and average aperture are the highest in the 1st set and lowest in the 3rd set, which is closely related to their mechanical causes. Specifically, the 1st set is mainly composed of tensile fractures, while the 3rd set is mainly composed of shear fractures. The aperture of fractures also increases with the slope altitude, with tensile fractures showing a more obvious trend than shear fractures. The aperture of tensile fractures is generally positively correlated with their trace length, while the relationship between the aperture of shear fractures and their trace length is not clearly established. The probability distribution of aperture for fractures of varying orientations differs, with the primary distributions being normal, log-normal, and gamma distributions.

Declaration of competing interest

The authors declare that they have no known competing financial interests or personal relationships that could have appeared to influence the work reported in this paper

Acknowledgments

This work was supported by the National Nature Science Foundation of China (Grant Nos. 42177139 and 41941017), the Natural Science Foundation Project of Jilin Province, China (Grant No. 20230101088JC). The authors would like to thank the anonymous reviewers for their comments and suggestions.

Appendix A. Supplementary data

Supplementary data to this article can be found online at https://doi.org/10.1016/j.jrmge.2023.07.010.

References

Azarafza, M., Asghari-Kaljahi, E., Akgün, H., 2017. Numerical modeling of discontinuous rock slopes utilizing the 3DDGM (three-dimensional discontinuity geometrical modeling) method. Bull. Eng. Geol. Environ. 76 (3), 989–1007.

Bar, N., Borgatti, L., Donati, D., Francioni, M., Salvini, R., Ghirotti, M., 2021. Classification of natural and engineered rock slopes using UAV photogrammetry for assessing stability. IOP Conf. Ser. Earth Environ. Sci. 833 (1), 012046.

Bostanci, H.T., Alemdag, S., Gurocak, Z., Gokceoglu, C., 2018. Combination of discontinuity characteristics and GIS for regional assessment of natural rock slopes in a mountainous area (NE Turkey). Catena 165, 487–502.

Cui, Z., Qi, S., Han, W., 2022. The role of weak bedding planes in the cross-layer crack growth paths of layered rocks. Geomech. Geophys. Geo-Energy Geo-Resour. 8 (1), 22.

Einstein, H.H., Veneziano, D., Baecher, G.B., O'Reilly, K.J., 1983. The effect of discontinuity persistence on rock slope stability. Int. J. Rock Mech. Min. Sci. Geomech. Abstr. 20 (5), 227–236.

Eshiet, K.I.-I., Sheng, Y., 2017. The role of rock joint frictional strength in the containment of fracture propagation. Acta Geotech 12 (4), 897–920.

Frash, L.P., Carey, J.W., Welch, N.J., 2019. Scalable En echelon shear-fracture aperture-roughness mechanism: theory, validation, and implications. J. Geophys. Res. Solid Earth 124 (1), 957–977.

Gentier, S., 1990. Hydromechanical behavior of a single natural fracture under normal stress. Hydrogeology 1, 327.

Gong, J., Rossen, W.R., 2017. Modeling flow in naturally fractured reservoirs: effect of fracture aperture distribution on dominant sub-network for flow. Petrol. Sci. 14 (1), 138–154.

Hakami, E., Barton, N., 1990. In: Barton, N., Stephansson, O. (Eds.), Aperture measurements and flow experiments using transparent replicas of rock joints, ROCK JOINTS. Taylor & Francis, ROTTERDAM, pp. 383–390.

Hakami, E., Stephansson, O., 1993. In: Ribeiroesousa, L., Grossmann, N. (Eds.), Experimental-technique for aperture studies of intersecting joints, Eurock 93, Lisboa, Portugal - Proceedings : Safety and Environmental Issues in Rock Engineering, vol. 1. Taylor & Francis, ROTTERDAM, pp. 301–308.

Hammah, R.E., Curran, J.H., 1998. Fuzzy cluster algorithm for the automatic identification of joint sets. Int. J. Rock Mech. Min. Sci. 35 (7), 889–905.

Huo, X., 2020. Development characteristics of Xiali clustered debris flow and its influence on route selection of Sichuan-Tibet railway. Railw. Eng. 60 (9), 146–150 (in Chinese).

ISRM, 1978. Suggested methods for the quantitative description of discontinuities in rock masses. Int. J. Rock Mech. Min. Sci. Geomech. Abstr. 15 (6), 319–368.

Iwano, M., Einstein, H., 1993. In: Ribeiroesousa, L., Grossmann, N. (Eds.), Stochastic-analysis of surface-roughness, aperture and flow in a single fracture, Eurock 93, Lisboa, Portugal - Proceedings : Safety and Environmental Issues in Rock Engineering, vol. 1. Taylor & Francis, ROTTERDAM, pp. 135–141.

Jiang, S., Ouyang, S., Feng, Z., Kang, Q., Haung, J., Yang, Z., 2021. Reliability analysis of jointed rock slopes using updated probability distributions of structural plane parameters. Rock Soil Mech. 42 (9), 2589–2599.

Johansen, K., Erskine, P.D., McCabe, M.F., 2019. Using unmanned aerial vehicles to assess the rehabilitation performance of open cut coal mines. J. Clean. Prod. 209, 819–833.

Keller, A., 1998. High resolution, non-destructive measurement and characterization of fracture apertures. Int. J. Rock Mech. Min. Sci. 35 (8), 1037–1050.

Kersten, T., Wolf, J., Lindstaedt, M., 2022. Investigations into the accuracy of the UAV system DJI Matrice 300 RTK with the sensors Zenmuse P1 and L1 in the hamburg test field. Int. Arch. Photogram. Rem. Sens. Spatial Inf. Sci. XLIII-B1-2022, 339–346.

Kumar, A.T.A., Majors, P., Rossen, W., 1997. Measurement of aperture and multiphase flow in fractures with NMR imaging. SPE Form. Eval. 12 (2), 101–107.

Lan, H., Tian, N., Li, L., Wu, Y., Macciotta, R., Clague, J.J., 2022. Kinematic-based landslide risk management for the Sichuan-Tibet Grid Interconnection Project (STGIP) in China. Eng. Geol. 308, 106823.

Lee, S., Kim, B., Baik, H., Cho, S.-J., 2022. A novel design and implementation of an autopilot terrain-following airship. IEEE Access 10, 38428–38436.

Li, B., Wang, J., Liu, R., Jiang, Y., 2021. Nonlinear fluid flow through three-dimensional rough fracture networks: Insights from 3D-printing, CT-scanning, and high-resolution numerical simulations. J. Rock Mech. Geotech. Eng. 13 (5), 1020–1032.

Li, Y., Xu, Q., Aydin, A., 2017. Uncertainties in estimating the roughness coefficient of rock fracture surfaces. Bull. Eng. Geol. Environ. 76 (3), 1153–1165.

Liu, J., Yang, H., Bai, J., Wu, K., Zhang, G., Liu, Y., Xiao, Z., 2021a. Numerical simulation to determine the fracture aperture in a typical basin of China. Fuel 283, 118952.

Liu, D., Ge, H., Shen, Y., Liu, H., Zhang, Y., 2021b. Experimental investigation on imbibition characteristics of shale with highly developed bedding fractures. J. Nat. Gas Sci. Eng. 96, 104244.

Liu, G., Yu, Q., Li, H., Li, J., Zhang, B., Wei, Y., 2019. Study on applicability of unmanned aerial vehicle mobile survey of open - pit mine in alpine region. Coal Sci. Technol. 47 (10), 43–50.

Liu, Y., Chen, J., Tan, C., Zhan, J., Song, S., Xu, W., Yan, J., Zhang, Y., Zhao, M., Wang, Q., 2022. Intelligent scanning for optimal rock discontinuity sets considering multiple parameters based on manifold learning combined with UAV photogrammetry. Eng. Geol. 309, 106851.

Lopes, J.A.G., Medeiros, W.E., La Bruna, V., De Lima, A., Bezerra, F.H.R., Schiozer, D.J., 2022. Advancements towards DFKN modelling: Incorporating fracture enlargement resulting from karstic dissolution in discrete fracture networks. J. Pet. Sci. Eng. 209, 109944.

Mazumder, S., Wolf, K.-H.A.A., Elewaut, K., Ephraim, R., 2006. Application of X-ray computed tomography for analyzing cleat spacing and cleat aperture in coal samples. Int. J. Coal Geol. 68 (3–4), 205–222.

Priest, S.D., Hudson, J.A., 1981. Estimation of discontinuity spacing and trace length using scanline surveys. Int. J. Rock Mech. Min. Sci. Geomech. Abstr. 18 (3), 183–197.

Priest, S.D., Hudson, J.A., 1976. Discontinuity spacings in rock. Int. J. Rock Mech. Min. Sci. Geomech. Abstr. 13 (5), 135–148.

Rahman, D.A., Sitorus, A.B.Y., Condro, A.A., 2021. From coastal to montane forest ecosystems, using drones for multi-species research in the tropics. Drones 6 (1), 6.

Reinhardt, M., Jacob, A., Sadeghnejad, S., Cappuccio, F., Arnold, P., Frank, S., Enzmann, F., Kersten, M., 2022. Benchmarking conventional and machine learning segmentation techniques for digital rock physics analysis of fractured rocks. Environ. Earth Sci. 81 (3), 71.

Ren, C., Shang, H., Zha, Z., Zhang, F., Pu, Y., 2022. Color balance method of dense point cloud in landslides area based on UAV images. IEEE Sensor. J. 22 (4), 3516–3528.

Salvini, R., Mastrorocco, G., Seddaiu, M., Rossi, D., Vanneschi, C., 2017. The use of an unmanned aerial vehicle for fracture mapping within a marble quarry (Carrara, Italy): photogrammetry and discrete fracture network modelling. Geomatics, Nat. Hazards Risk 8 (1), 34–52.

Salvini, R., Vanneschi, C., Coggan, J.S., Mastrorocco, G., 2020. Evaluation of the use of UAV photogrammetry for rock discontinuity roughness characterization. Rock Mech. Rock Eng. 53 (8), 3699–3720.

Schellhaas, H., 1999. A modified Kolmogorov-Smirnov test for a rectangular distribution with unknown parameters: computation of the distribution of the test statistic. Stat. Pap. 40 (3), 343–349.

Shi, 2021. Study on Characteristics of the Xiali 2# Debris Flow and its Potential Perniciousness on a Engineering Project. Southwest Jiaotong University, Chengdu (in Chinese).

Shi, H., Hu, X., Wen, Q., Zhang, X., 2021. Debris flow development characteristics and dynamic process numerical simulation of Xiali 2# gully on the proposed Sichuan-Tibet railway. J. Geol. Hazards Environ. Preserv. 32 (3), 39–46 (in Chinese).

Song, C., Nakashima, S., Kido, R., Yasuhara, H., Kishida, K., 2021. Short- and long-term observations of fracture permeability in granite by flow-through tests and comparative observation by X-ray CT. Int. J. GeoMech. 21 (9), 04021151.

Song, S., Wang, Q., Chen, J., Li, Y., Zhang, W., Ruan, Y., 2017. Fuzzy C-means clustering analysis based on quantum particle swarm optimization algorithm for the grouping of rock discontinuity sets. KSCE J. Civ. Eng. 21 (4), 1115–1122.

Song, S., Zhao, M., Zhu, C., Wang, F., Cao, C., Li, H., Ma, M., 2022. Identification of the potential critical slip surface for fractured rock slope using the Floyd algorithm. Rem. Sens. 14 (5), 1284.

Sun, Z., Wang, L., Zhou, J.-Q., Wang, C., 2020. A new method for determining the hydraulic aperture of rough rock fractures using the support vector regression. Eng. Geol. 271, 105618.

Torkan, M., Janiszewski, M., Uotinen, L., Baghbanan, A., Rinne, M., 2022. Photogrammetric method to determine physical aperture and roughness of a rock fracture. Sensors 22 (11), 4165.

Tsang, Y., Tsang, C., 1990. In: Barton, N., Stephansson, O. (Eds.), Hydrological characterization of variable-aperture fractures, ROCK JOINTS. Taylor & Francis, ROTTERDAM, pp. 423–431.

Wang, F., Yan, X., Wang, M., Zhang, X., Niu, X., Wang, Q., 2020. Universal three-point model of generating a new coordinate system and its application. J. Jilin Univ. Technol. Ed. 50 (1), 324–332 (in Chinese).

Wu, F., 1993. Principles of Statistical Mechanics of Rock Masses. China University of Geosciences Press, Wuhan (in Chinese).

Wu, F., Wu, J., Bao, H., Li, B., Shan, Z., Kong, D., 2021. Advances in statistical mechanics of rock masses and its engineering applications. J. Rock Mech. Geotech. Eng. 13 (1), 22–45.

Xiao, L., Li, K., 2011. Characteristics of the nuclear magnetic resonance logging response in fracture oil and gas reservoirs. New J. Phys. 13 (4), 045003.

Xiu, C., Li, Z., Duan, H., Lu, X., Ma, T., Shan, C., 2021. Plane accuracy of aero-photogrammetry without image control points of DJI PHANTOM 4 RTK UAV. IOP Conf. Ser. Earth Environ. Sci. 734 (1), 012003.

Yeo, I.W., De Freitas, M.H., Zimmerman, R.W., 1998. Effect of shear displacement on the aperture and permeability of a rock fracture. Int. J. Rock Mech. Min. Sci. 35 (8), 1051–1070.

Zhan, L., Guo, X., Sun, Q., Chen, Y., Chen, Z., 2021. The 2015 Shenzhen catastrophic landslide in a construction waste dump: analyses of undrained strength and slope stability. Acta Geotech 16 (4), 1247–1263.
Zhang, G., Wang, X., Liang, Y.-C., Liu, J., 2010. Fast and robust spectrum sensing via Kolmogorov-Smirnov test. IEEE Trans. Commun. 58 (12), 3410–3416.
Zheng, J., Kulatilake, P.H.S.W., Shu, B., Sherizadeh, T., Deng, J., 2014. Probabilistic block theory analysis for a rock slope at an open pit mine in USA. Comput. Geotech. 61, 254–265.

Mingyu Zhao obtained his MSc degree in Geomatics Engineering from Jilin University, China, in 2020. He is currently pursuing a PhD in Geological Engineering at Jilin University. His research interests include: (1) the engineering geological applications of UAV photogrammetry and digital close-range photogrammetry technologies; and (2) the non-contact fine interpretation and characterization of complex rock mass structures. He has participated in multiple projects funded by the National Natural Science Foundation of China.